Hindawi
Advances in Materials Science and Engineering
Volume 2020, Article ID 5353690, 18 pages
https://doi.org/10.1155/2020/5353690

Research Article

Thermomechanical Analysis of the Effects of Water Distribution on Cracks during Vertical Continuous Casting under Soft Reduction Conditions

Yu Yao,[1,2] Bo Wang,[1,2] Shanshan Liu,[1,2] Liping Zhong,[1,2] Shiyi Shen,[1,2] Zheng Chen,[1,2] and Jieyu Zhang[1,2]

[1]*State Key Laboratory of Advanced Special Steel, Shanghai University, Shanghai, China*
[2]*School of Materials Science and Engineering, Shanghai University, Shanghai, China*

Correspondence should be addressed to Bo Wang; bowang@shu.edu.cn

Received 20 August 2019; Revised 12 December 2019; Accepted 27 December 2019; Published 25 January 2020

Academic Editor: Pavel Lejcek

In the production process of continuous casting slab, the unreasonable secondary cooling system can lead to serious crack defects. This study focuses on the problem of cracks in nuclear power stainless steel produced by vertical continuous casting under soft reduction conditions. Based on the actual production process parameters, the thermomechanical finite element model was established to investigate the effects of water distribution in the secondary cooling zones on cracks by using ProCAST. The results show that the stress concentration is obvious under the original process, especially the positions of 4 mm below the wide surface and 6 mm below the narrow surface. It is easy to generate cracks, and the area with the highest hot-tearing index is approximately 26 cm^2. In addition, the secondary cooling system is adjusted based on the existing problems of the original process. The temperature of the casting slab rises by about 15°C at the solidification end point, and the length of the liquid core increases by about 0.5 m when the quantity of the water flow decreases in zone 2 and zone 3. The stress concentration is alleviated, and the possibility of cracking is reduced. Especially, it is evident that the proportion of water on the loose side margin increases from 40% to 45%, while the proportion of water on the fixed side margin of zone 3 is adjusted from 56% to 60%.

1. Introduction

The soft reduction is the main modern continuous casting process technology, which can greatly alleviate or even eliminate the central segregation and center porosity and ensure the high compactness of the solidification structure of the slab [1–4]. Research by relevant scholars has found that the inner quality of wide-thick slab was significantly improved with the liquid core around 1/8 location of slab width increased after the water flux was decreased around the slab corner [5]. The centerline segregation and "V-" type segregation can be improved significantly after the application of soft reduction to the bloom [6]. Wu et al. [7] found that the rotation speed of the front roller (V_f) is faster than that of the reduction roller (V_r), which can effectively suppress the porosity elongation, and the effect of HR on improving the bloom internal porosity could be effectively promoted. When they investigated the closure behavior of internal porosity in continuous casting bloom during heavy reduction, they found that the application of a convex roll helps to reduce internal porosity more efficiently [8].

The secondary cooling system plays a vital role in the quality of the slab in the process of vertical continuous casting under soft reduction [9]. For an unreasonable secondary cooling system will cause surface cracks, internal cracks, and bulging, etc., which seriously affect the quality of the slab [10–13].

The nuclear power stainless steel is the most conspicuous in the production of many steel grades because it has good comprehensive mechanical properties, excellent strength at high temperatures, and stress corrosion resistance and is widely used in the industry [14–16]. However, a domestic

steel plant often has defects such as cracks and pits in the process of producing nuclear power stainless steel by vertical continuous casting at present. Due to the extremely complicated production process of continuous casting, which involves not only the mass, heat, and momentum transfer but also the deformation of the casting slab caused by phase transition, thermal stress, and mechanical force, it is difficult to reproduce by experimental methods [17, 18], while numerical simulation can control the complex process conditions, and it has higher safety factor with far less cost, which is more conducive to the long-term development of enterprises [19].

Many scholars have studied the numerical simulation of the optimization of the secondary cooling system of continuous casting process. Zhang et al. [20] presented an unequal interval arrangement of nozzles (UIAN) in the casting direction of the secondary cooling process for continuous casting of the round billets, which can uniform the surface temperature of the round billets and eliminate the midway cracks. Meanwhile, Hou et al. [21] developed a dynamic secondary cooling control model which can automatically adjust the secondary cooling flow according to the slab casting parameters and maintain the slab surface temperature closer to the target value. It can also improve the surface cracks and central segregation. In addition, Feng et al. [22] established the optimal construct of water distribution in the secondary cooling zone, which decreases the heat loss rate and the surface temperature gradient of the slab simultaneously. Fan et al. [23] proposed a uniform secondary cooling pattern (USCP) for minimizing the surface reheating of the strand, and it shows that the appropriate extension of the secondary cooling zone can significantly reduce the longitudinal surface reheating of the strand. Gong et al. [24] investigated the effects of different solidification rates on the microstructures, microsegregation, and mechanical properties of cast superalloy K417 G. It indicates that the slowest cooling rate of 0.84°C/s showed the best comprehensive mechanical properties. However, the current research neglects to regulate the water quantity in the specific zones where cracks are more likely to occur, which cannot effectively analyze the reasons of crack initiation and expansion and suppress the quality defects of the slab caused by unreasonable secondary cooling water distribution from the root cause.

This paper mainly focuses on the nuclear power stainless steel produced by a vertical steel continuous casting machine. Based on the high-temperature mechanical properties of the slab and the soft reduction process parameters and the solidification characteristics of the slab, the mathematical model was established to simulate the influence of water distribution on cracks by ProCAST. The possibility of crack occurrence is reduced by optimizing water distribution in the secondary cooling section, and the simulation results would be helpful in further improving the quality of the steel.

2. Model Formulation

2.1. Mathematical Model. Due to the heat transfer along the casting direction in the continuous casting process, which can be neglected for it takes up about 3%~6% of the total heat [25]. Therefore, the thermomechanical behavior of continuous casting process is simulated by using the thin-slicing method in this paper. In order to save the calculation time, the model takes half of the casting slab section for calculation; the size of the slice is 650 mm × 200 mm × 3 mm. Among them, the width, casting direction, and thickness along the slab are, respectively, the coordinates X, Y, and Z directions, and the grid element is a hexahedral grid with a size of 6.5 mm × 6.5 mm. Figure 1 shows the schematic diagram of the slice space coordinates and the geometry model.

2.2. Model Equations

2.2.1. Heat Transfer Equation. Considering the complexity of the continuous casting production process, the heat transfer equations are simplified with the assumptions that the heat dissipation along the casting direction is neglected; the convective heat transfer of the molten steel is treated by the equivalent enhancement of the thermal conductivity; the surface temperature is the same as the pouring temperature of the molten steel and evenly distributed; the same cooling zone is evenly cooled in the second cooling section; the influencing factors such as heat transfer of the idle rollers are comprehensively reflected in the heat transfer coefficient. Therefore, the heat conduction differential equation can be simplified as a two-dimensional unsteady heat transfer problem, which can be expressed as

$$\rho c \frac{\partial T}{\partial t} = \frac{\partial}{\partial x}\left[k_{\text{eff}}\frac{\partial T}{\partial x}\right] + \frac{\partial}{\partial z}\left[k_{\text{eff}}\frac{\partial T}{\partial z}\right] + S, \quad (1)$$

where ρ is the density, kg/m^3; c is the specific heat capacity, J/(kg·°C); S is the inner heat resource, W/m^3; k_{eff} is the thermal conductivity, W/(m·°C); and T is the temperature, °C.

Using the specific heat method to deal with latent heat of solidification process, S is given by

$$S = \rho L \frac{\partial f_s}{\partial t}, \quad (2)$$

where L represents latent heat of fusion J/kg and f_s is the solid fraction.

2.2.2. Thermal-Elastic-Plastic Model. During the solidification of the casting slab, the variation of stress can effectively predict the location and change trend of slab cracks. Many stress models are applied to the simulation of stress field. Considering the complexity of the model and the accuracy of the simulation results, the thermal-elastic-plastic model is adopted, assuming that the slab is a continuous medium and isotropic, and the geometric size changes caused by slab deformation are ignored.

Considering the effect of temperature on stress [26], the total strain increment includes thermal strain increment ε_t, elastic strain increment ε_e, and plastic strain increment ε_p:

$$\{\varepsilon\} = \{\varepsilon_e\} + \{\varepsilon_p\} + \{\varepsilon_t\}. \quad (3)$$

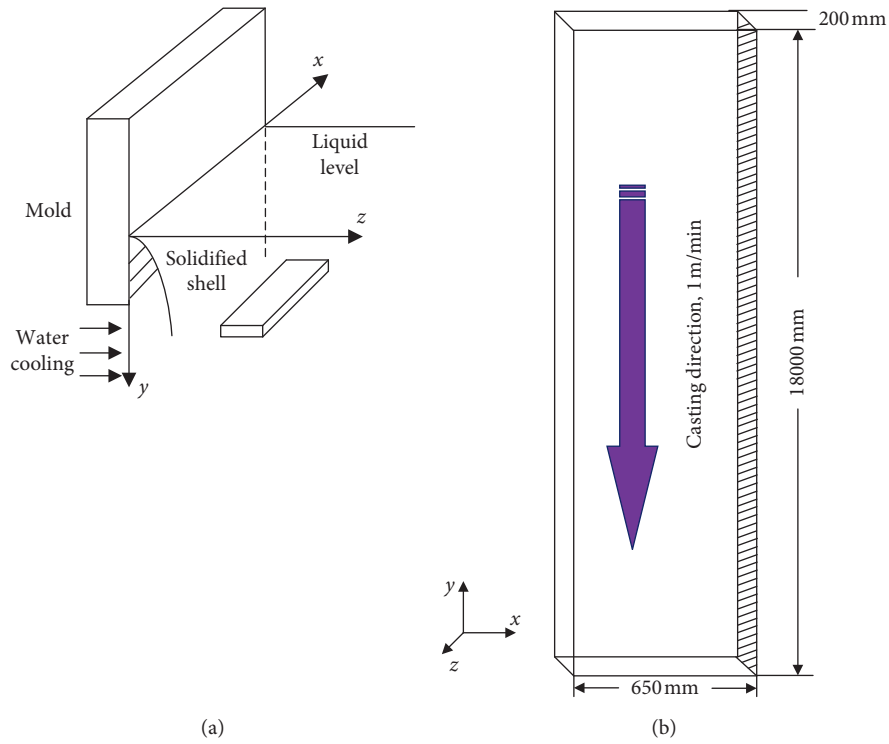

Figure 1: Schematic diagram: (a) simulated slice space coordinates; (b) geometry model.

The effective stress can be expressed as

$$\overline{\sigma}_{\text{eff}} = \frac{1}{\sqrt{2}}\sqrt{(\sigma_1-\sigma_2)^2+(\sigma_2-\sigma_3)^2+(\sigma_3-\sigma_1)^2}, \quad (4)$$

where σ_1, σ_2, and σ_3 represent three principal stresses, respectively.

Yield criterion is governed by the von Mises criterion [27]:

$$f = \sqrt{\frac{3}{2}\|s-x\|-k}, \quad (5)$$

where f, s, and k represent yield function of the yield surface, deviatoric stress, and characterizes isotropic hardening, respectively; x is the back stress which controls the kinematic hardening.

Elastic stage: its stress satisfies the yield inequality $f(\sigma_{ij}) \le 0$, and the elastic part is governed by Hooke's law:

$$\sigma = E\varepsilon_e, \quad (6)$$

where E is the elastic modulus.

Plastic stage: its stress satisfied the yield function $f(\sigma_{ij}) = 0$, and the plastic part follows the Prandtl–Resus flow rule:

$$\varepsilon_p = \gamma\frac{\partial f}{\partial \sigma}, \quad (7)$$

where γ is the plastic multiplier determined with the aid of the consistency condition, $f = 0$.

For isotropic hardening, k can be chosen as

$$k = \sigma_0 + H\overline{\varepsilon}_p, \quad (8)$$

where σ_0 is the yield stress, H is the plastic modulus, and $\overline{\varepsilon}_p$ is the effective plastic strain.

2.2.3. Hot-Tearing Prediction Model. During the process of continuous casting, the occurrence of hot tearing seriously affects the quality of the product, from surface defects to breakout accidents. Therefore, it is very important to predict the occurrence of hot-tearing defects in the slab. The ProCAST software provides two hot-tearing prediction models: HTI model and HCS model. HTI model, which is based on the total strain, is mainly used to predict the hot-cracking defects of the casting slab in this paper [28, 29]. The model used on modified Gurson's constitutive and measures the hot-tearing sensitivity at different joints when the solid fraction is between 50% and 99%. It can be shown as follows:

$$l_{ht} = \int_{t_c}^{t}\sqrt{\frac{2}{3}\varepsilon_p : \varepsilon_p}\,\mathrm{d}\tau\,(t_c \le t \le t_s), \quad (9)$$

where t_c and t_s is the time when the coherency temperature and solidus temperature are reached.

2.3. High-Temperature Mechanical Properties and Soft Reduction Parameters

2.3.1. High-Temperature Mechanical Properties. The high-temperature mechanical properties reflect the ability of the casting slab to resist deformation under the behavior of external stress during solidification. In order to get the high-temperature mechanical properties of the material,

thermal-mechanical simulator (Gleeble-1500D, Dynamic Systems Inc, New York State, USA) was used to test the high-temperature tensile. By studying the relationship between mechanical properties and temperature of nuclear power stainless steel, Young's modulus [30], yield strength, tensile strength, Poisson's ratio [25], and plastic modulus are obtained, as shown in Figure 2.

2.3.2. Soft Reduction Parameters

(1) Reduction Zone. The final stage of solidification of the continuous casting slab is an important basis for determining the position of starting to apply soft reduction. The determination of the final stage of solidification is based on the actual production process parameters of the factory. By simulating the nuclear power stainless steel solidification heat transfer process of the continuous casting slab, one can accurately determine the solidification end point.

At present, there are no specific values to determine the reduction zone. For different steel types and section sizes, the reduction zone is different [31]. Based on the production parameters from the test correction, the reduction parameters of steel plant are obtained. The determination of the reduction zone in this study is determined by Takahashi [32]; the solid-phase ratio is in the range of 0.3–0.7.

(2) Reduction Rate. The commonly used reduction rate is the semiexperience formula by summarizing and sorting many field test data [33]:

$$R_v = D\left|\frac{W}{D}\right|^{-0.25} \cdot \left(T_L - T_S\right)^{0.5} \cdot 10^{-3}, \tag{10}$$

where D is the slab shell thickness, mm and W is the slab width, mm.

(3) Reduction Amount. The reduction amount is composed of natural solidification shrinkage and actual reduction amount. The solidification shrinkage of the casting slab should be considered in the design of the soft reduction parameters and make an appropriate heat shrinkage system of roll gap for a more accurate model. The thermal expansion coefficient of nuclear power stainless steel in Figure 3(a) is obtained from the literature, and the solidification shrinkage of the casting slab is calculated according to its thermal expansion coefficient [30], as shown in Figure 3(b).

Based on the data provided by the factory, the actual reduction amount is 10 mm. Assuming that the distribution of reduction amount is linear within the reduction zone, the reduction amount is calculated according to the distribution of the solid phase fraction at the center of the casting slab [34], and the formulation is shown as follows:

$$R_i = \frac{f_i - f_{\text{start}}}{f_{\text{end}} - f_{\text{start}}} \cdot R, \tag{11}$$

where R_i is the reduction amount of the ith idle roller in the reduction zone, mm; R is the actual reduction amount, mm; f_{start} and f_{end} represent the solid fraction of start and end points of the reduction zone; and f_i is the solid fraction of the ith idle roller in the reduction zone.

Table 1 shows the reduction amount of different idle rollers under soft reduction.

2.4. Initial and Boundary Conditions. The initial temperature of molten steel is 1491°C, the degree of superheat is 35°C, and the casting speed is 1.0 m/min.

During the solidification process of continuous casting slab, heat is continuously transferred to the surrounding environment. The boundary conditions of the heat transfer can be divided into three parts: the mold, the second cooling zone, and the air-cooling zone. In the secondary cooling zone, there is a difference between the fixed side and the loose side. The cooling intensity between the center and the margin of zone 1 and zone 3 is different, as shown in Figure 4(a). Figure 4(b) shows the idle rollers' arrangement.

The average heat flux in the mold can be expressed as

$$\overline{q} = \frac{Q}{S}, \tag{12}$$

where S is the effective heat exchange area of the mold, m^2 and Q is the total heat energy taken away by cooling water per unit time, J/s.

In this paper, temperature difference between inlet and outlet water is measured to calculate the total heat taken away by cooling water:

$$Q = q_w \cdot C_w \cdot \Delta T_w, \tag{13}$$

where q_w is the water flow rate, kg/s, C_w is the heat capacity of water, J/(kg·°C), and ΔT_w is the temperature difference between the inlet and the outlet of the mold, 6°C.

At the secondary cooling zone, the boundary condition can be expressed as

$$q = h\left(T_b - T_{\text{amb}}\right), \tag{14}$$

where T_b is the surface temperature, °C, T_{amb} is the ambient temperature, 20°C, and h is the average heat transfer coefficient, kW/(m·°C).

The heat transfer between the casting slab and the idle rollers is considered when determining the heat transfer coefficient h, and Nozaki formula [35] is adopted:

$$h = \frac{1.57W^{0.451}\left(1 - 0.0075T_w\right)}{\alpha}, \tag{15}$$

where, W is the spray cooling flux, L/(m^2·s), α is a machine-dependent calibration factor, the value of the roller zone is 5.0 and the remaining zones are 5.56, and T_w is the temperature of the spray, 25°C.

For the narrow surface of the continuous casting slab, only the roller zone is cooled by the water spray, and the rest is air-cooling. The radiant heat transfer also happens between the slab surface and the ambient environment, and the formula is shown as follows [36]:

$$q = \sigma e\left[\left(T_b + 273\right)^4 - \left(T_w + 273\right)^4\right], \tag{16}$$

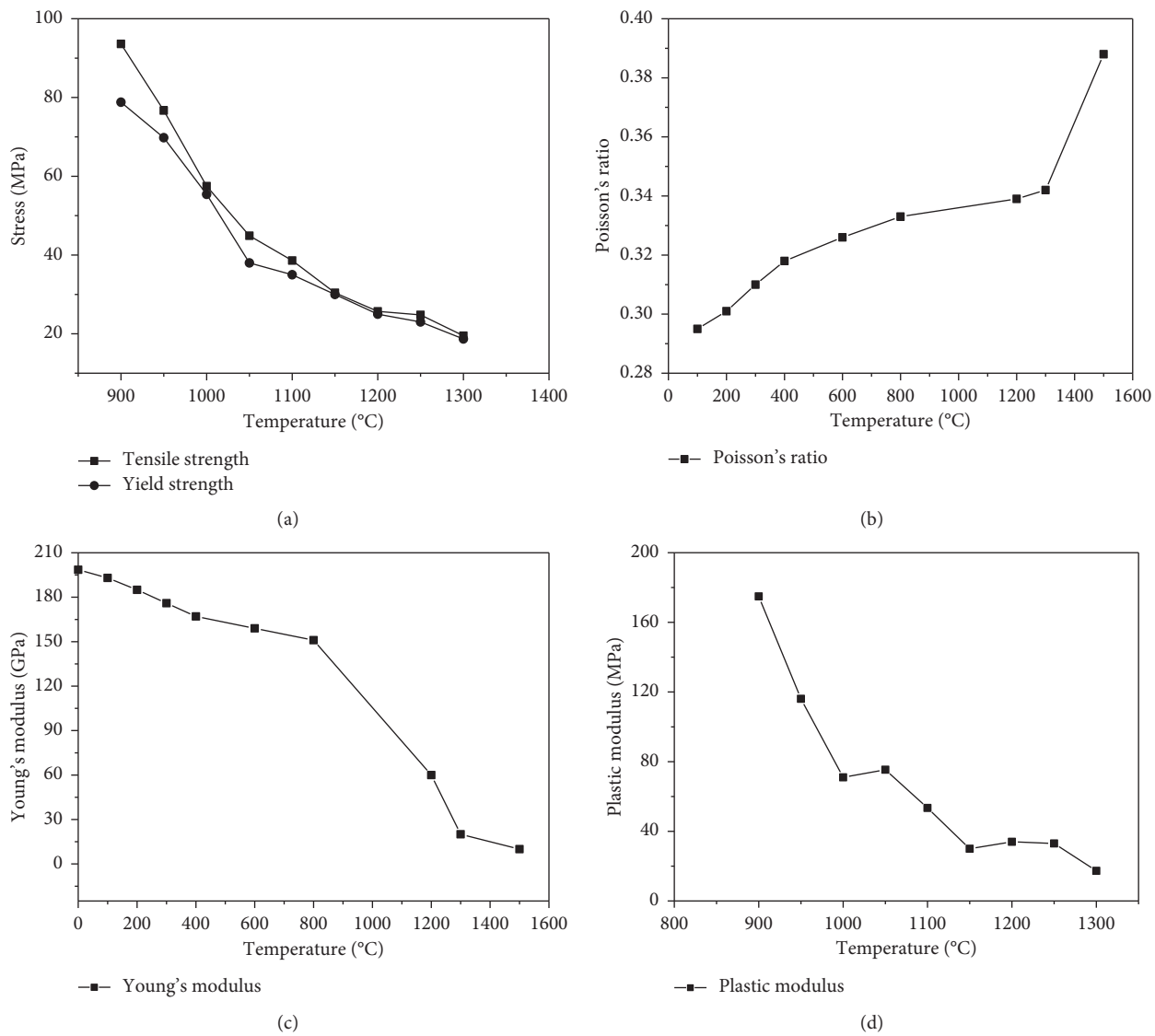

Figure 2: High-temperature mechanical properties of nuclear power stainless steel. (a) Yield strength and tensile strength. (b) Poisson's ratio. (c) Young's modulus. (d) Plastic modulus.

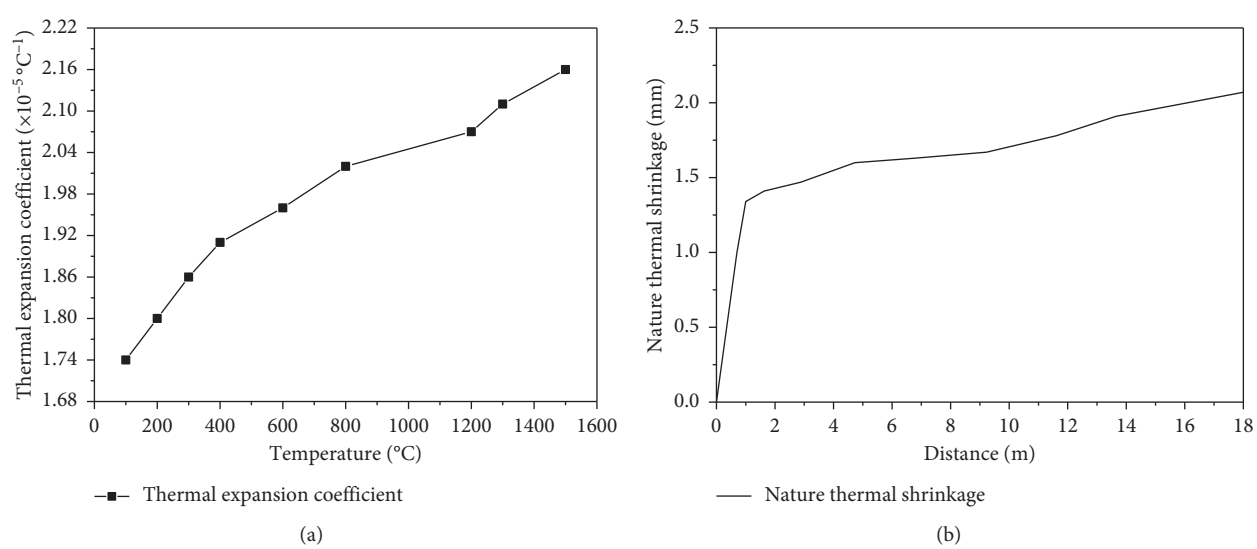

Figure 3: Solidification characteristics of nuclear power stainless steel. (a) Thermal expansion coefficient. (b) Nature thermal shrinkage.

Table 1: The reduction amount of different idle rollers in the reduction zone.

Idle roller number	Roll diameter (mm)	Distance from meniscus (m)	Reduction amount (mm)
1	250	6.16	0.38
2	250	6.46	1.68
3	250	6.78	2.68
4	250	7.08	3.68
5	250	7.38	4.68
6	250	7.68	5.40
7	250	7.98	6.15
8	250	8.28	7.33
9	250	8.58	7.95
10	250	8.88	8.60
11	300	9.22	10.00

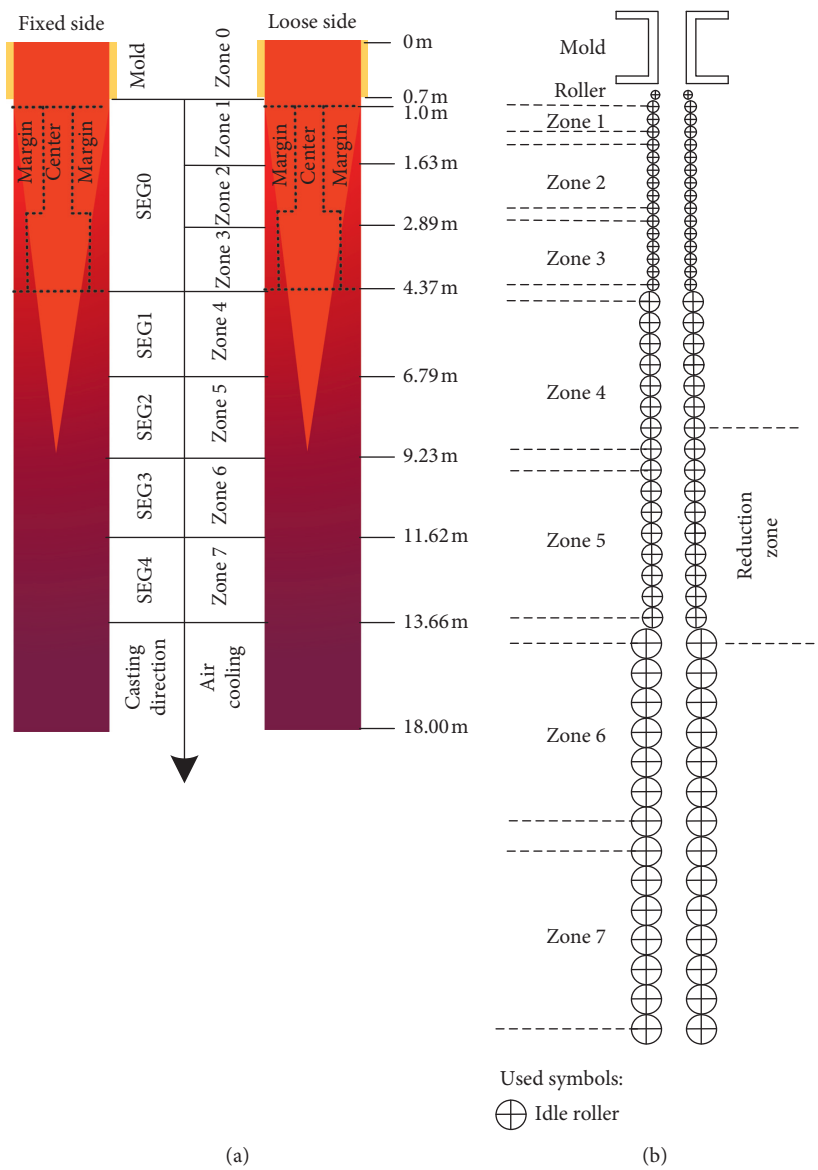

Figure 4: Schematic diagram of cooling sections: (a) total diagram; (b) idle rollers' arrangement.

where σ is the Stefan–Boltzmann constant, 5.67×10^{-8} W/($m^2 \cdot K^4$) and e is the emissivity coefficient, 0.8.

The displacement boundary condition is used by the stress calculated model constraint. In the casting direction, the displacement is set to 0 for the cross section is not affected by the idle rollers. The effects of soft reduction and solidification contraction were taken into account when setting the displacement boundary condition of the wide surface. It can be expressed by the reduction amount in Table 1.

2.5. Material. The chemical composition of nuclear power stainless steel was obtained by ICP test, as shown in Table 2.

The solidus and liquidus temperature are 1380°C and 1456°C, respectively. During the solidification of the continuous casting slab, the relationship between solid fraction and temperature adopted in this paper is as follows:

$$f_s = \sqrt{\frac{T_L - T}{T_L - T_S}} \left(T_c \leq T \leq T_s\right), \tag{17}$$

where T_S is the solidus temperature, °C and T_L is the liquidus temperature, °C.

Other thermophysical parameters (as shown in Table 3) such as thermal conductivity, specific heat, and density were obtained from [37].

3. Results and Discussion

3.1. Reliability Verification of Simulation. In order to verify the accuracy of simulation results, the above cooling boundary conditions were used to simulate the temperature field of continuous casting process. As shown in Figure 5, the actual target temperature of the factory at the center of the wide surface at the exit of each zone was compared with the numerical simulation results. The temperature field of simulation results is well matched with the actual target temperature distribution, which verifies the accuracy of heat transfer coefficient selected in this paper and the rationality of boundary conditions.

3.2. Analysis of Original Process Results. In the process of continuous casting, the cooling intensity in the secondary cooling zone plays an important role, which determines the quality of the casting slab to a large extent [38]. Therefore, the reasonable secondary cooling water distribution can effectively reduce the possibility of casting defects and ensure the efficient production of continuous casting process. Firstly, the process of original process was analyzed, and then the secondary cooling water distribution is adjusted according to the existing problems of the original process.

Figure 6 shows the distribution of cross-sectional temperature and solidification fraction at each outlet of the casting slab. It can be seen intuitively from the cloud diagram that the corner temperature of the casting slab drops first, and the temperature is lower than that of the wide and narrow surface on the same cross section. With the solidification of the casting slab, the temperature at the outlet of each zone gradually decreases, and the obvious contraction phenomenon occurs in the width direction. As can be seen from the cloud diagram of solidification fraction of the casting slab, the thickness of the casting slab shell increases and grows to the center with the cooling going on. After entering zone 7, the liquid core gradually disappears, and the casting slab is completely solidified.

In order to quantitatively analyze the temperature behavior of the casting slab in the process of solidification, this paper selects the four characteristic positions of slab corner, narrow surface center, wide surface center, and the center of the casting slab for analysis. Figure 7(a) shows the changes in the temperature field along the casting direction at the characteristic positions. The heat exchange of the liquid core to outside is small, the release of latent heat of solidification offsets the casting slab heat dissipating, and the temperature of the casting slab center changes along the casting direction is relatively flat. After the internal liquid core disappears, the temperature drops sharply. Due to the uneven distribution of chilling effect in different zones, it is easy to cause thermal stress concentration and have a possibility of cracking. Both wide and narrow surfaces simultaneously dissipate heat at the corner of the slab, making the temperature of the corner to drop fastest. Since the narrow surface is out of the roller, the cooling method changes from aerosol cooling to air cooling, the temperature of the narrow surface and corner rises.

To prevent the breakout accidents caused by the static pressure of molten steel, it is generally required that the shell thickness at the outlet of the mold should be over 13 mm [39]. In this paper, the solid fraction of 0.7 is chosen as the solid-liquid interface. Figure 7(b) shows the growth curve of the wide-surface slab shell. The slab shell in the mold grows rapidly, and it reaches 14.8 mm at the outlet of the mold, meeting the requirements of safety slab shell thickness. The solidification end point is approximately about at 12.8 m.

In the process of solidification heat transfer, there is a large temperature gradient in the interior of the slab and on the surface of the slab shell, which makes the natural shrinkage of each part of the casting slab restrict each other and generate thermal stress [40]. Excessive and uneven thermal stress may lead to crack initiation or make the original cracks expand. The effective stress can be used to judge whether the casting slab has cracks caused by yield damage, while the first principal stress can determine whether it has cracks caused by brittle fracture [41].

It can be seen in Figure 8 that the effective stress in the corner of the slab is obviously higher than that on the wide and narrow surface, and the stress concentration phenomenon occurs first. With the growth of the shell, the effective stress on both wide and narrow surfaces of the slab gradually extends from the surface to the inside of the casting slab. The effective stress distribution becomes more and more uneven when entering zone 3 and zone 4; this may easily lead to narrow-surface cracks and cracks of the corner. Along the direction of casting, the first principal stress on the shell gradually becomes larger. When the casting slab leaves the mold, the wide surface is subjected to compression stress, while it is subjected to the maximum tensile stress at 4 mm

Table 2: Chemical composition of nuclear power stainless steel.

Elements	Cr	Ni	Mn	Si	C	Cu	Co	P	Fe
Wt.%	18.59	9.18	0.93	0.27	0.021	0.096	0.063	0.01	Others
GB/T	18.00–20.00	9.00–12.00	<2.00	<1.00	<0.030	<1.00	<0.10	<0.030	

Table 3: Thermophysical parameters.

	Solid zone ($T \le T_s$)	Mushy zone ($T_s < T < T_L$)	Liquid zone ($T_L \le T$)
Thermal conductivity	19.62 W/(m·K)	$k_{\text{eff}} = k_S + k_L(1 - f_s)$	$k_{eff} = m \cdot k_S$
Specific heat	711.62 J/(kg·K)	$C_{\text{eff}} = C_S f_S + C_L(1 - f_s) - L(\partial f_s/\partial T)$	837.20 J/(kg·K)
Density	7200 kg/m^3	$\rho_{\text{eff}} = \rho_S f_S + \rho_L(1 - f_s)$	6900 kg/m^3

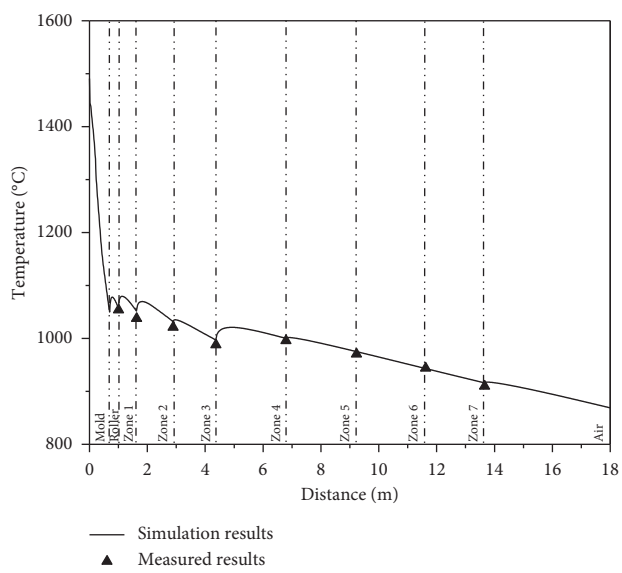

Figure 5: Comparison between the simulation results and results measured by the inbuilt model of the casting machine at the exit of each zone.

away from the wide surface. During the solidification of the casting slab, cracks are easy to occur where the tensile stress is large, so this region is selected as the feature position to study the possibility of cracking [41]. The slab is subjected to compression stress at 6 mm from the narrow surface, in contrast to the outer surface, which is also an area with high incidence of subsurface cracks.

According to the change rule of the effective stress of the corner, the narrow surface center, the wide surface center, and the center of the casting slab along the casting direction in Figure 9, the variation of effective stress of the slab is quantitatively analyzed. As shown in the picture, the effective stress of the corner, narrow surface center, and wide surface center is on the rise inside the mold. The temperature drop rate in the corner of the slab is higher than that on the narrow and wide surface, with the effective stress reaching 127 MPa. Therefore, cracks are likely to occur in the corner. From the roller to zone 1, the effective stress of the corner shows a downward trend for its temperature rises, and the thermal stress concentration is alleviated. From zone 2 to zone 3, the effective stress on the wide surface, narrow surface, and corner of the slab shows an upward trend. Due to the cooling effect on the surface of the slab makes the shrinkage of the shell intensified and generates tensile stress, resulting in obvious stress concentration, and it is easy to germinate cracks. In zone 4, effective stress of the slab corner decreases first and then shows a smooth upward trend. This is because the temperature of the slab corner recovery in zone 4 and Young's modulus and the plastic modulus decrease quickly.

In the later stage, as the temperature of the slab decreases and the soft reduction is applied, the effective stress at the corner tends to rise again. The uneven distribution of the effective stress will cause the possibility of cracks to a large extent. After entering zone 5, the effective stress of the narrow surface reaches 61.4 MPa, which exceeds the tensile strength at the corresponding temperature, resulting in the cracks on the narrow surface. The effective stress of the wide surface center reaches 52.9 MPa, which is closer to the strength limit of the slab. Therefore, the design of reasonable secondary cooling system makes the temperature distribution on the outer surface uniform, which is very important to reduce the possibility of cracking of the slab.

According to the cloud diagram of the first principal stress, there is a large stress concentration at 4 mm below the wide surface and 6 mm below the narrow surface, so the two positions are selected as characteristic positions for analysis. As shown in Figure 10(a), the first principal stress at 4 mm below the wide surface increases from the roller to zone 4 and then decreases inside the mold, and the peak reaches at a distance of 0.015 m from the narrow surface, where it is very likely to initiate cracks under the tensile stress. The first principal stress value changes rapidly from zone 2 to zone 3, which can be improved by adjusting the cooling intensity of zone 2 and zone 3 to make the temperature uniform, thereby reducing the degree of change of the first principal stress. From zone 5 to the outlet of zone 7, the first principal stress shows a decreasing trend, and two peaks are formed at 0.015 m and 0.06 m from the narrow surface.

Figure 10(b) shows the distribution of the first principal stress at 6 mm below the narrow surface along the thickness of the slab. The position that is 5 mm~7 mm away from the outer surface of the wide surface is a high-risk region where cracks occur for its value of the first principal stress reaches the maximum. From zone 2 to zone 3, the principal stress of the slab changes from the main tensile stress to the main compressive stress, and the change trend is obvious for the

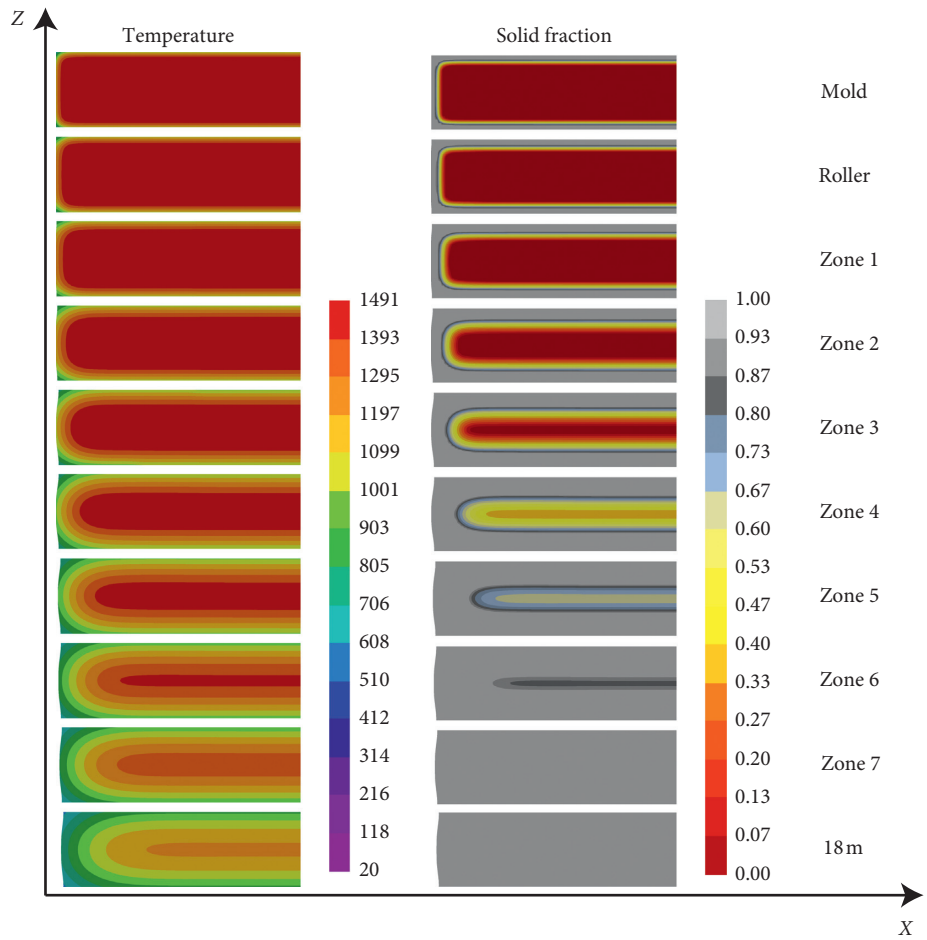

Figure 6: Cloud diagram of temperature field and solid fraction of the casting slab at cross section.

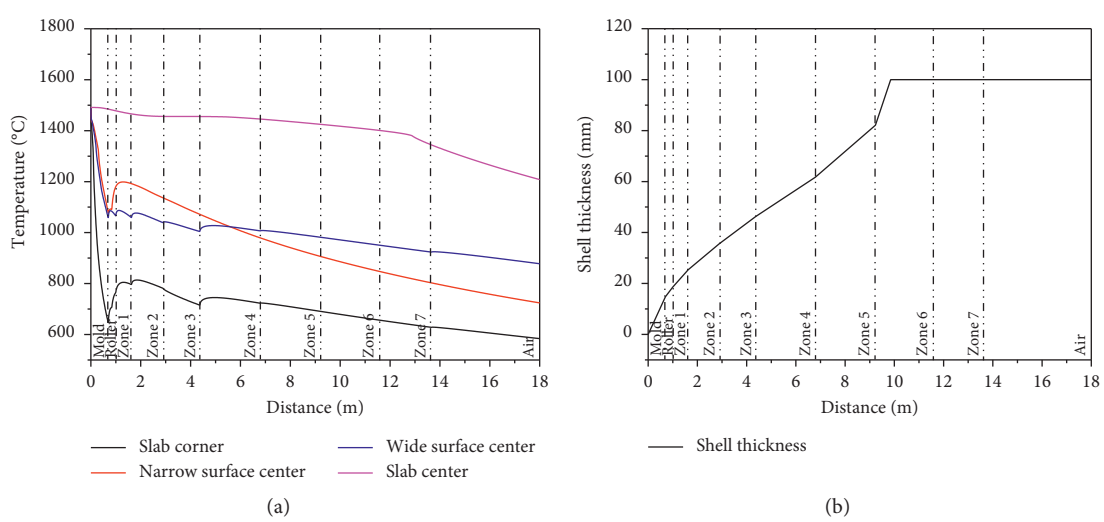

Figure 7: Temperature field simulation results. (a) Temperature change curves at characteristic positions. (b) The variable trend of thickness of the shell.

bulge deformation. As the cooling progresses, the slab shrinks significantly, resulting in the compressive stress from the zone 2 to zone 3 to gradually decrease and become the tensile stress.

Figure 11 shows a cloud diagram of the distribution of the hot-tearing index at each outlet of the slab. It can be found that when the slab is out of the mold, the hot tearing first appears at the corner of the slab, and both sides of the

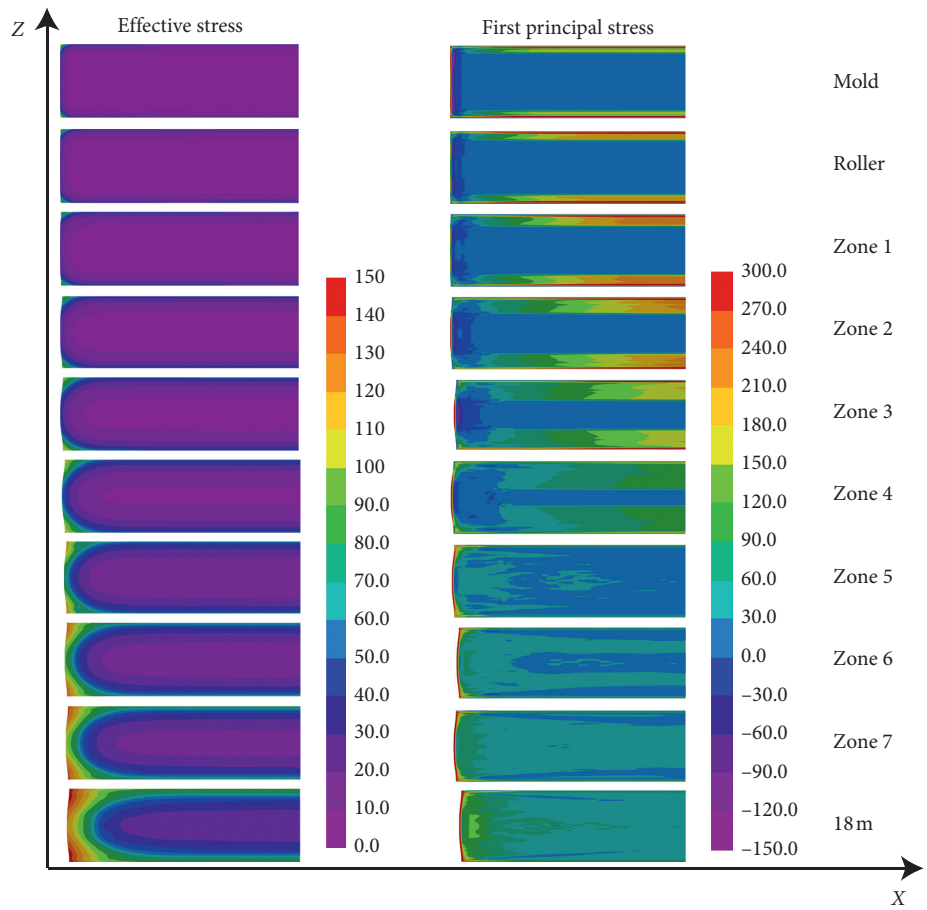

Figure 8: The cloud diagram of the effective stress and the first principal stress distribution on the cross section of the outlet of each zone.

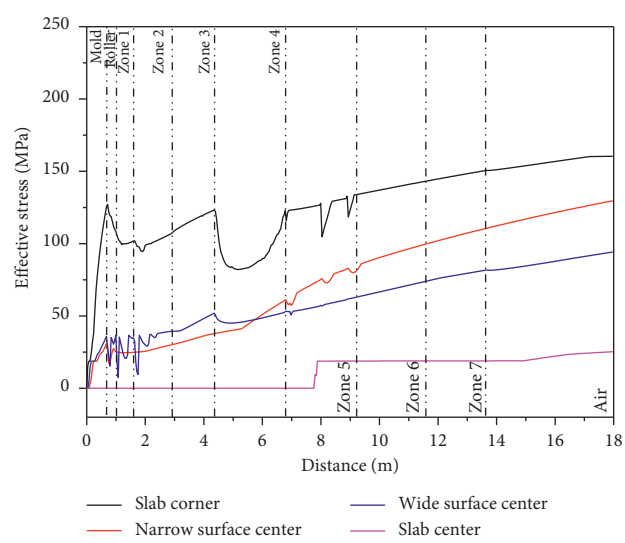

Figure 9: Distribution of effective stress curves at the characteristic positions.

wide surface are symmetrically distributed. The closer to the inside of the slab, especially to the front edge of the solid-liquid interface, the greater the hot-tearing index is. When the slab is out of zone 6, the hot-tearing index does not change substantially, and the region of hot tearing is no longer expanded and is basically stable. The shape of the region with the highest thermal cracking index (the thermal cracking index ranges from 0.0918 to 0.0984) is elliptic. The area of the casting slab in this region is approximately 26 cm^2, and the possibility of internal hot tearing is very high.

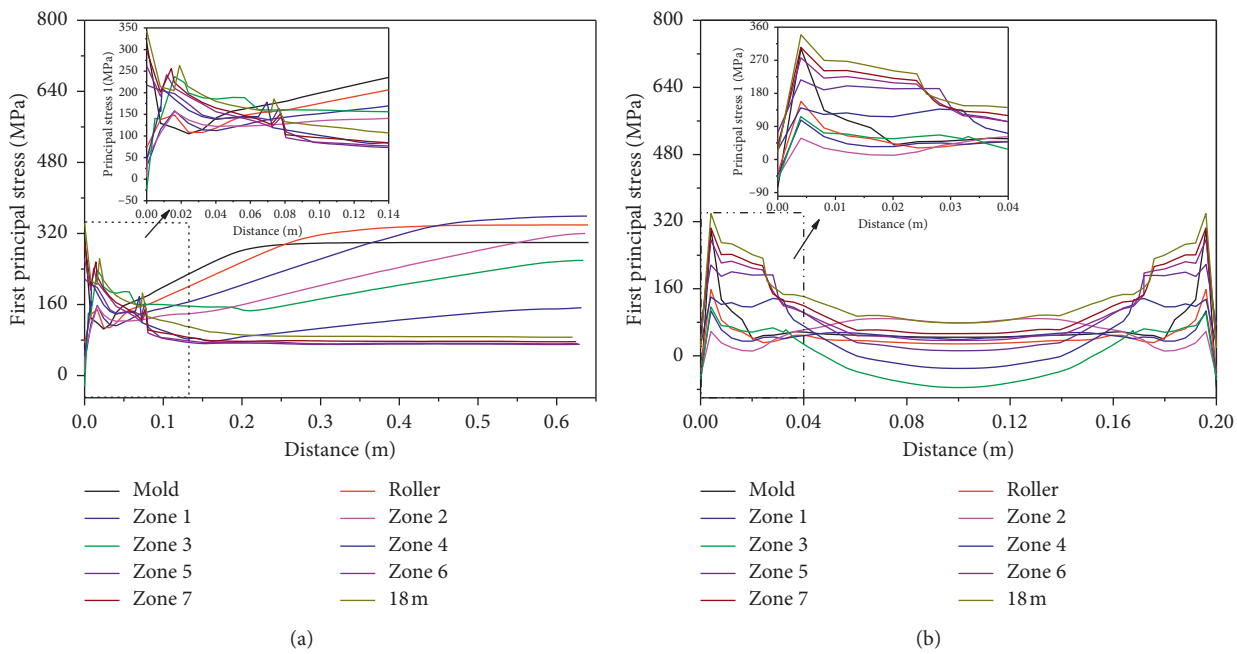

Figure 10: First principal stress curves of the casting slab. (a) 4 mm below the wide surface. (b) 6 mm below the narrow surface.

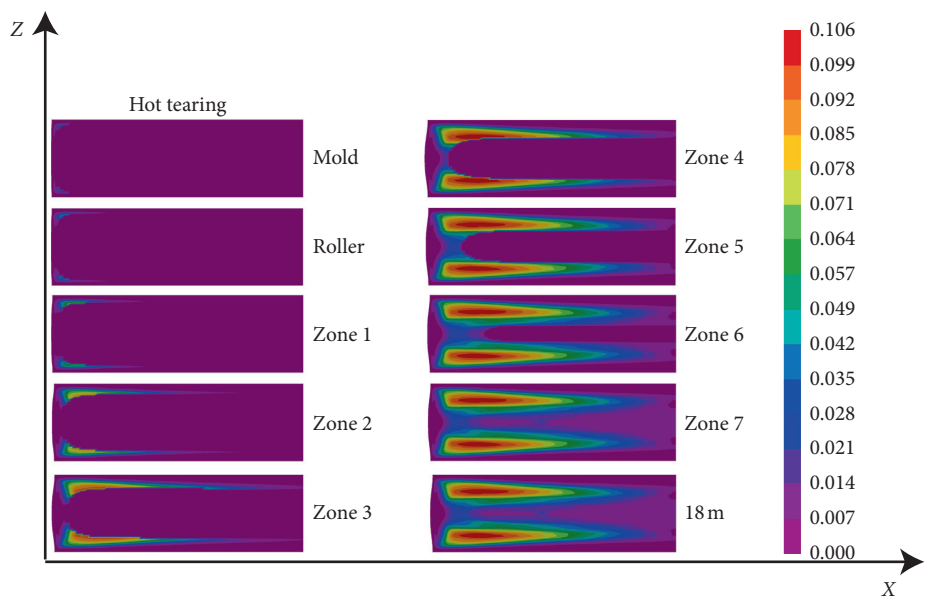

Figure 11: Hot-tearing index of the casting slab at cross section.

3.3. Effect of Cooling Conditions on the Secondary Cooling Zone. According to the simulation results of the original process, the effective stress on the outer surface of the slab is on the rise from zone 2 to zone 3, the stress concentration is more obvious, and the first principal stress changes rapidly and its distribution is uneven. Bulge deformation was formed on the outer surface of the narrow surface, and the possibility of cracking is high. In view of the problems in the original process, the possibility of cracking is reduced by adjusting the cooling intensity in zone 2 and zone 3. Due to the difference of cooling intensity between the margin and center in zone 2 and zone 3, the difference is also considered in the adjustment of water distribution. The specific schemes of distribution of water are shown in Table 4.

It can be seen from Figure 12 that the gap of temperature change between the adjustment schemes and the original process is not obvious until entering zone 5. This is due to the slow heat transfer from the solidified shell of the slab. When the slab is completely solidified, the temperature difference at the same position is about 15°C. Due to the decrease of cooling intensity and heat transfer capacity in zone 2 and zone 3, the solidification process of the casting

Table 4: Distribution of water under different water distribution schemes.

Secondary cooling zone	Original process (L·min^{-1})	Scheme one (L·min^{-1})	Scheme two (L·min^{-1})	Scheme three (L·min^{-1})
Roller N	22.8	22.8	22.8	22.8
Roller FL	87.0	87.0	87	87
Zone 1 FLC	37.9	37.9	37.9	37.9
Zone 1 FLM	56.9	56.9	56.9	56.9
Zone 2 FLC	44.3 (42%)	30.5 (42%)	31.95 (45%)	39.6 (55%)
Zone 2 FLM	59.1 (58%)	41.2 (58%)	39.01 (55%)	32.4 (45%)
Zone 3 FC	18.4 (44%)	13.7 (44%)	12.69 (40%)	18.4 (60%)
Zone 3 FM	23.4 (56%)	17.4 (56%)	19.04 (60%)	12.3 (40%)
Zone 3 LC	25.1 (60%)	22.6 (60%)	18.87 (55%)	13.7 (45%)
Zone 3 LM	16.7 (40%)	15.4 (40%)	15.44 (45%)	16.7 (55%)

N: narrow surface; F: fixed side; L: loose side; C: center; M: margin.

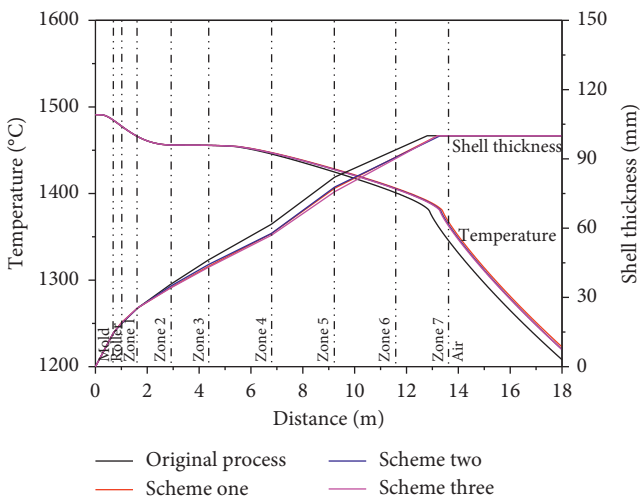

Figure 12: The curves of center temperature and slab shell growth under different water distribution schemes.

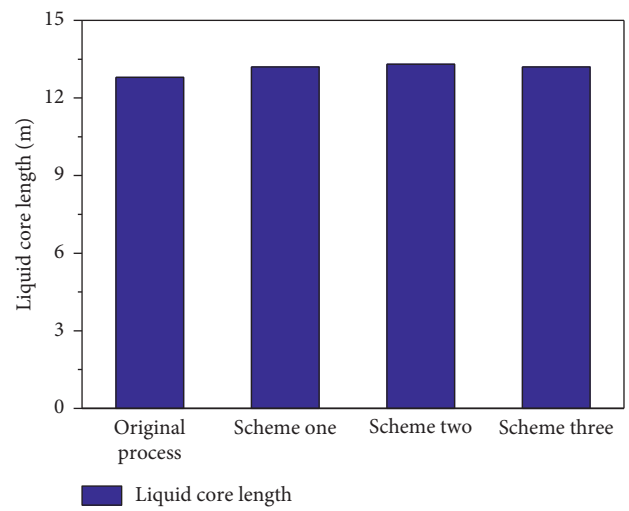

Figure 13: The liquid core length under different water distribution schemes.

slab slows down, resulting in the growth of the casting slab shells beginning to differ from the original process after entering zone 3.

Figure 13 shows the comparison of the liquid core lengths under different water distribution schemes. The smaller the cooling intensity, the longer the liquid core length. The liquid core length of scheme two is increased by 0.5 m compared with the original process.

In order to quantitatively analyze the change of temperature gradient, three characteristic lines were taken from the center of the wide surface, narrow surface, and the corner of the casting slab along the direction of casting. As can be seen from Figure 14(a), due to the proper decrease of cooling intensity in zone 2 and zone 3, the temperature distribution of the wide surface in zone 1 and zone 2 changes from the original downward trend to a temperature recovery trend. In zone 3, the temperature distribution of scheme one and scheme two is relatively uniform. Therefore, at the end of zone 3, the stress concentration phenomenon is alleviated and the stress peak disappears. The stress value decreases from 50.4 MPa to 37.7 MPa, greatly reducing the possibility of crack initiation. The temperature of scheme three decreases too fast in zone 2 and zone 3, resulting in the stress peak to still exist and cracks to occur and expand.

As shown in Figure 14(b), the effect of reducing the cooling intensity of the narrow surface center in zone 2 and zone 3 is weak. Only when the casting slab enters zone 5, the slight difference in temperature causes the effective stress fluctuation. Due to the narrow surface of the casting slab is cooled by aerosol, the heat exchange is larger than the rest of the air-cooled areas, and the relatively thick narrow surface is 200 mm, so adjusting the wide-face cooling intensity has little effect on temperature distribution of the narrow surface.

From Figure 14(c), the temperature of the slab corner in zone 2 and zone 3 shows an upward trend. At the outlet of zone 2, the temperature rises from 780°C to 838°C, 811°C, and 895°C. The effective stress in zone 2 decreases correspondingly from 106.3 MPa to 88.1 MPa, 98.5 MPa, and 80.1 MPa, and the tendency of cracking in zone 2 decreases significantly. It is worth noting that the effective stress distribution in the corner of the casting slab changes significantly, and the effective stress distribution in zone 4 is uniform by reducing the water quantity in zone 2 and zone 3. In the later stage, the temperature of the slab corner is generally 20% higher than that under the original process, and the effective stress decreased by 6 MPa.

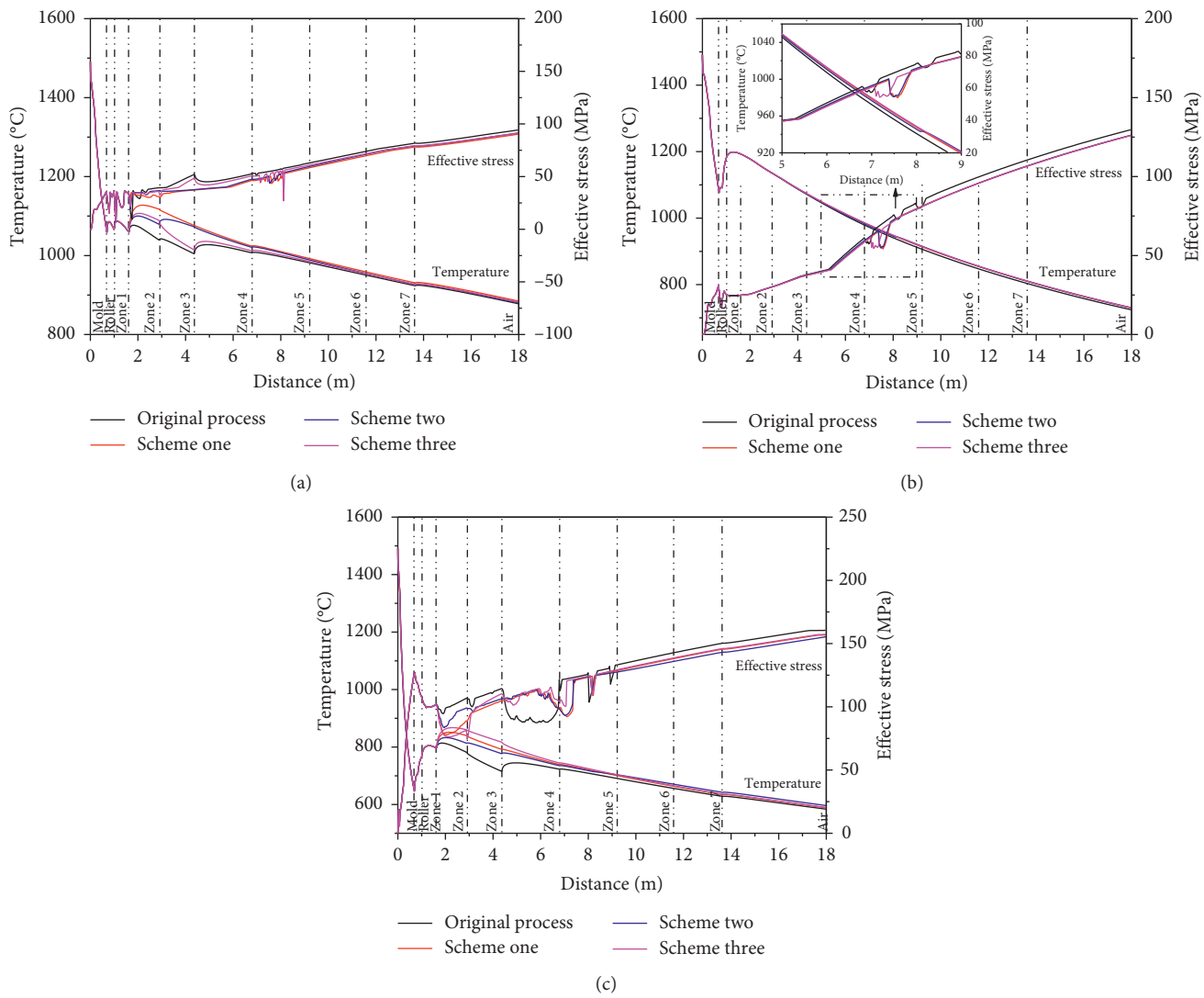

Figure 14: The curves of temperature and effective stress under different water distribution schemes. (a) Wide surface center. (b) Narrow surface center. (c) Corner.

Since the adjustment schemes of cooling intensity are aimed at zone 2 and zone 3, the first principal stress varies greatly in zone 2 and zone 3, and the other zones have a relatively minor impact. Zone 2 and zone 3 are mainly studied here. As can be seen from Figure 15, reducing the cooling intensity in zone 2 and zone 3 will decrease the first principal stress. By adjusting the distribution of water, the stress peaks at 0.015 m and 0.06 m from the narrow surface are significantly decreased at the outlet of zone 3, which significantly reduces the crack initiation. The corner of the casting slab receives heat dissipation from both wide surface and narrow surface, causing the corner temperature to decrease rapidly compared to the wide and narrow surfaces in the original process. It makes uneven temperature distribution on the surface of the casting slab and initiates cracks. It can be found that the first principal stress can be greatly reduced by decreasing the water quantity at the margin of zone 3. When the proportion of the edge is adjusted to 40%, the first principal stress is the lowest.

It can be seen from Figure 16 that the first principal stress along the thickness direction is almost symmetrically distributed. The closer to the center of the narrow surface, the lower the first principal stress. According to the temperature results above, this position at 6 mm below the narrow surface is the solidified shell, which is affected by the solidification shrinkage; the outer surface of the wide surface is subjected to compressive stress. The slab temperature gradient is large along the thickness direction, and the internal and external shrinkage of the slab is inconsistent, which makes the internal tensile stress.

When the water quantity in zone 2 is decreased, the value of the first principal stress at the outlet of zone 2 increases. When the proportion of water at the margin of zone 2 is 55%, the first principal stress rises to the maximum. When the cooling intensity in zone 2 and zone 3 is simultaneously reduced, the peak value of the first principal stress in zone 3 and zone 4 increases, resulting in the possibility of narrow-surface subsurface cracks to increase accordingly. However,

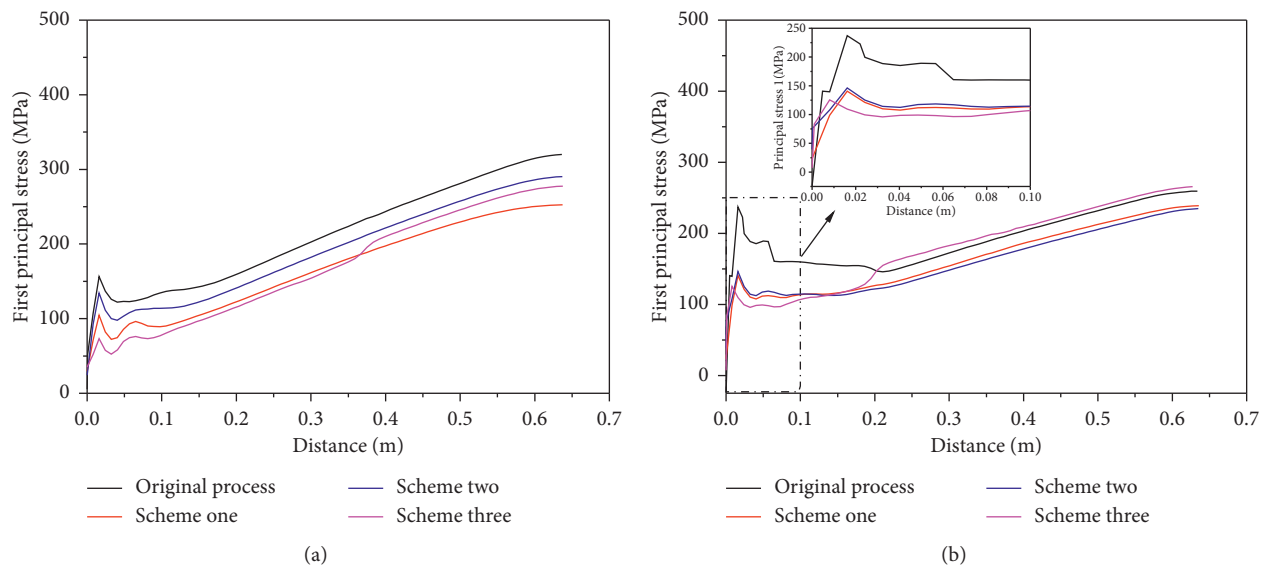

Figure 15: Comparison of the first principal stress at 4 mm below the wide surface under different water distribution schemes. (a) Outlet of zone 2. (b) Outlet of zone 3.

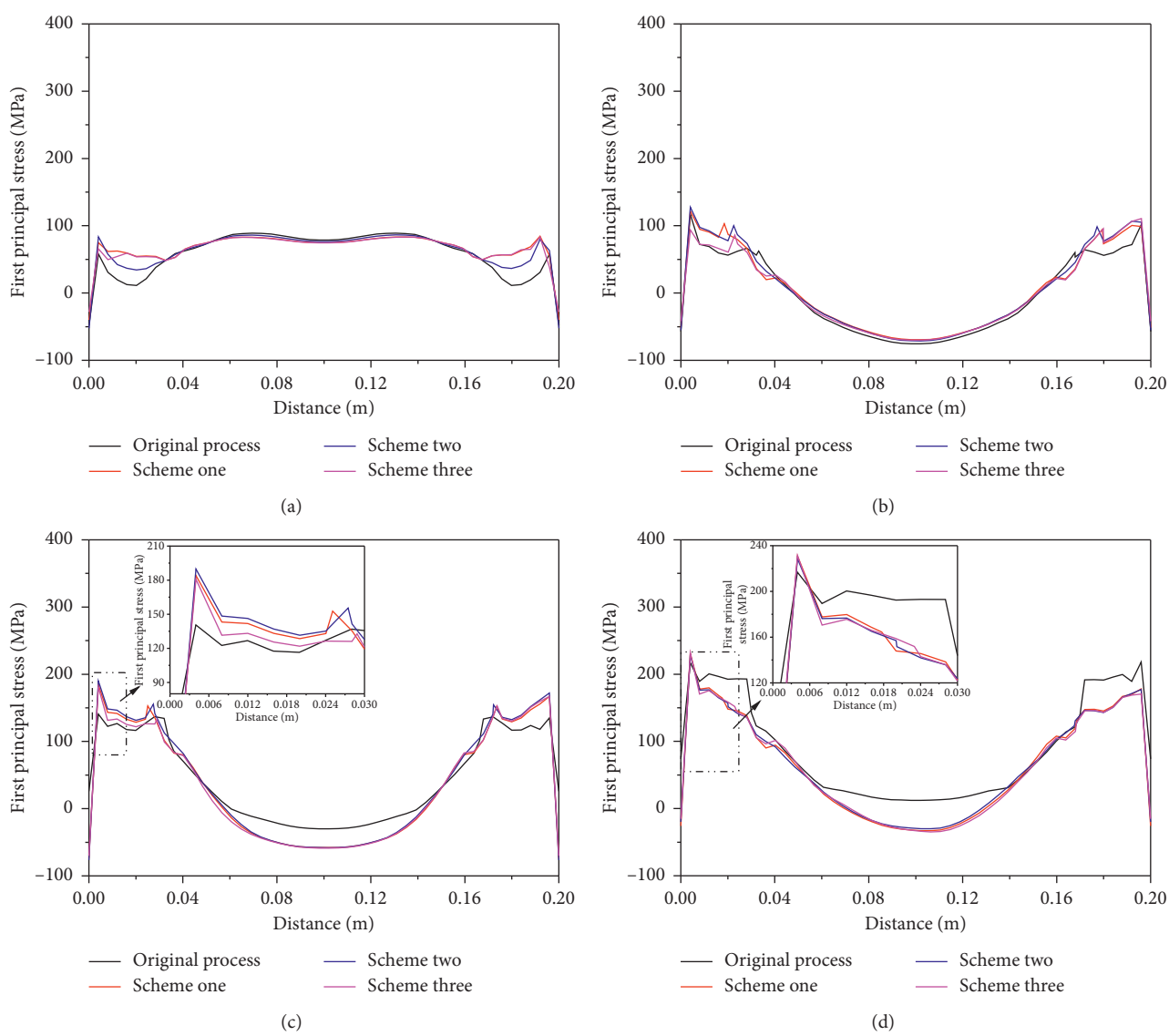

Figure 16: Continued.

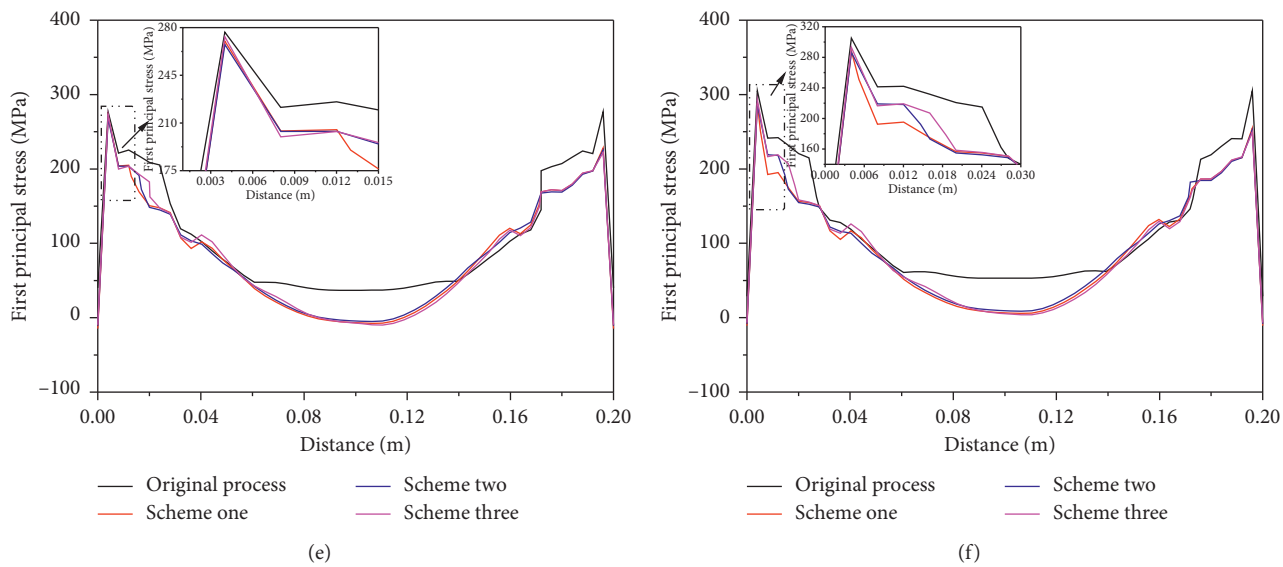

Figure 16: Comparison of the first principal stress at 6 mm below the narrow surface under different water distribution schemes. (a) Outlet of zone 2. (b) Outlet of zone 3. (c) Outlet of zone 4. (d) Outlet of zone 5. (e) Outlet of zone 6. (f) Outlet of zone 7.

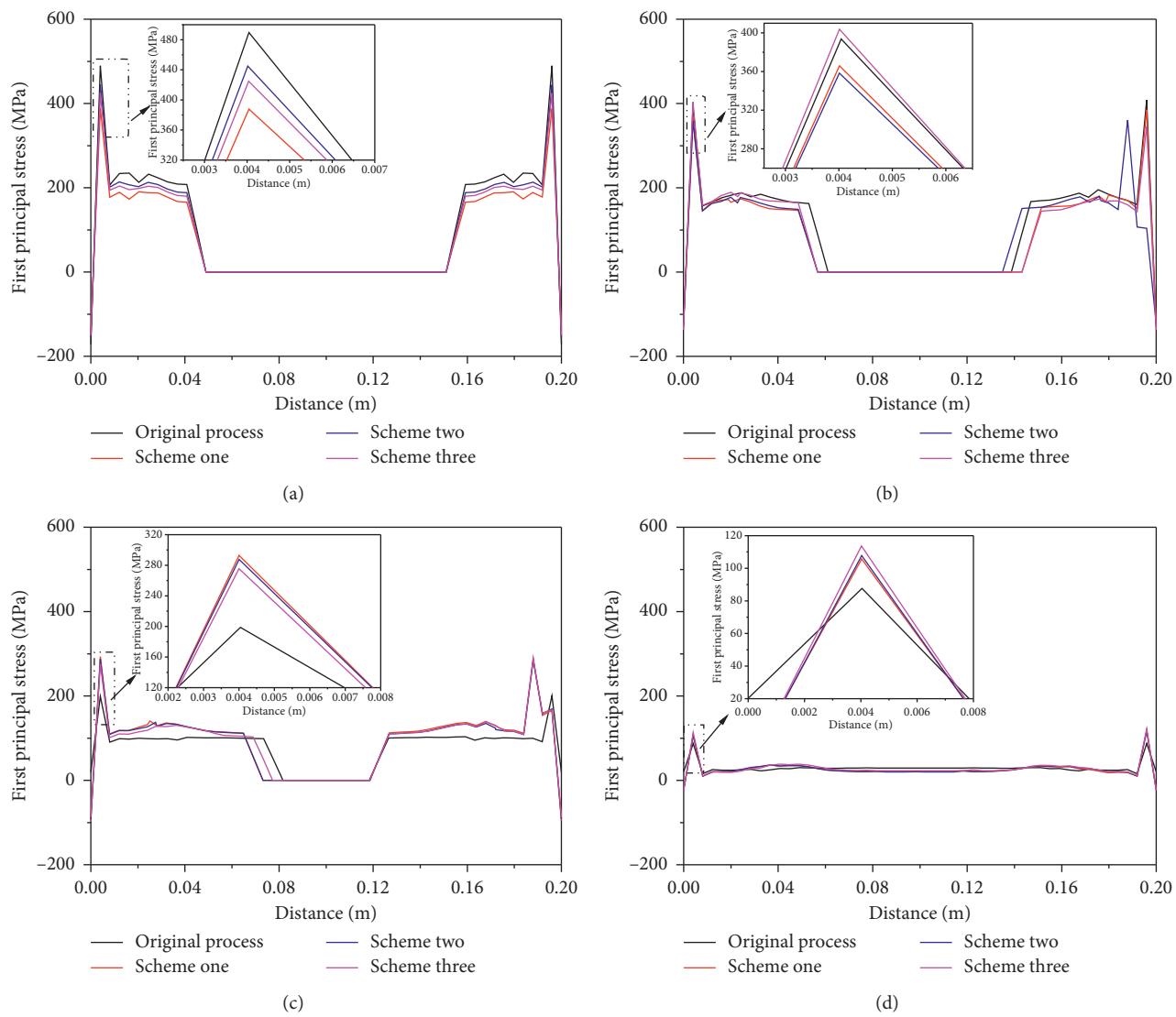

Figure 17: Comparison of the first principal stress at the narrow surface symmetric plane under different water distribution schemes. (a) Outlet of zone 2. (b) Outlet of zone 3. (c) Outlet of zone 4. (d) Outlet of zone 5.

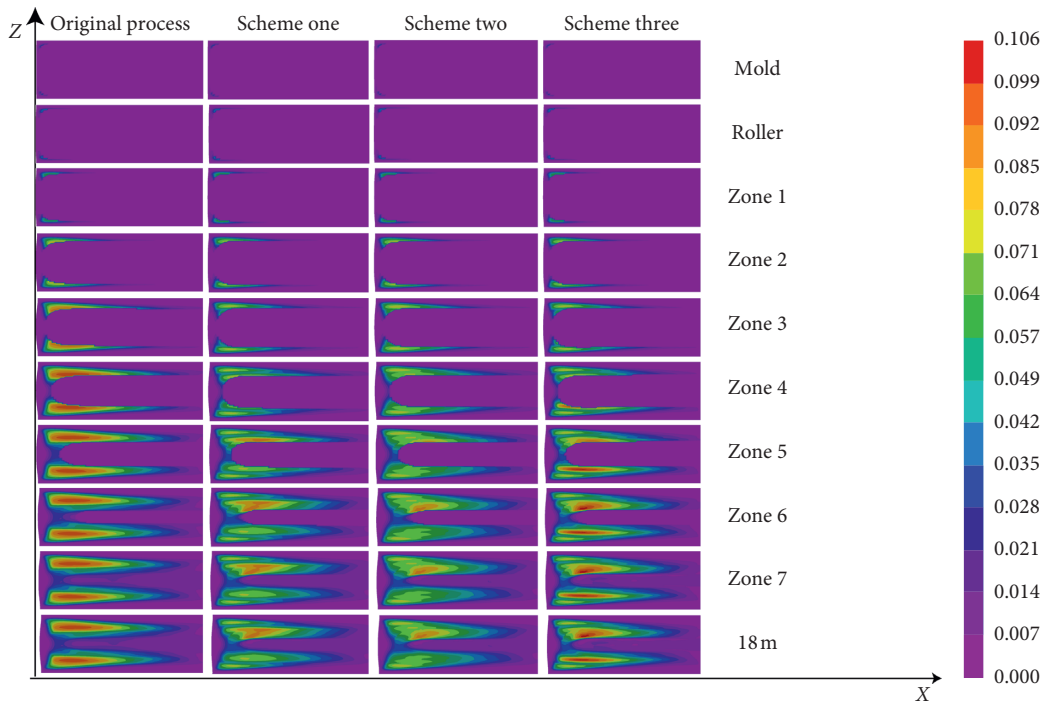

Figure 18: Hot-tearing distribution at the outlet of each zone under different water distribution schemes.

at the outlet of zone 5, zone 6, and zone 7, the peak of the principal stress disappeared at 0.02 m to 0.04 m from the wide surface, which reduces the risk of cracking.

Figure 17 shows the distribution of the first principal stress along the thickness direction at the outlet of each zone under different water distribution schemes at the narrow surface symmetric plane. According to the simulation results of the original process, the maximum value of the first principal stress is obtained at about 4 mm~5 mm away from the outer surface of the wide surface; it is the high-risk region where cracks occur. When cooling intensity in zone 2 and zone 3 is reduced, the peak value of first principal stress at the outlet of zone 2 and zone 3 also decreases correspondingly. Especially when the proportion of water in the center of zone 2 is 55%, the peak value of the first principal stress in zone 2 is the minimum. When the slab is at the outlet of zone 4, zone 5, zone 6, and zone 7, it can be clearly seen from the enlarged figure that the first principal stress has an upward trend compared with the original process, especially the changes of first principal stress in zone 4 and zone 5.

Figure 18 shows the cross-sectional cloud diagram of the distribution of hot tearing at the outlet of each zone under different cooling intensity schemes. It can be seen that when the slab is out of zone 2, the proportion of water at the margin of zone 2 decreased, and the distribution of the cracks at the outlet of zone 2 is narrowed in the width direction. After leaving zone 3, the hot-tearing index is significantly decreased, and the possibility of cracking in this region still decreases compared with the original process. Since the adjustment of cooling intensity in zone 3 is divided into the fixed side and the loose side, the distribution of the cracks is irregularly symmetrical. As shown in scheme two, when the water quantity of the center and margin of the fixed side is adjusted from 44%: 56% of the original process to 40%: 60% and the loose side is adjusted from 60%: 40% to 55%: 45%, the hot-tearing index becomes smaller. Overall, appropriately reducing the cooling intensity in zone 2 and zone 3 will significantly decrease the index of hot tearing, which will reduce the possibility of cracks.

4. Conclusions

In this paper, the thermomechanical finite element model of nuclear power stainless steel solidification process was established. Numerical simulations are carried to investigate the effects of the water distribution on cracks of nuclear power stainless steel in the vertical casting soft reduction process by ProCAST. Based on the results, the following conclusions can be summarized.

The positions which are under the wide surface with 4 mm and under the narrow surface 6 mm are more likely to generate cracks for its obvious stress concentration under the original process. The area with the highest hot-tearing index is elliptical and is approximately 26 cm^2, which is prone to generate internal cracks. The distribution of effective stress and the first principal stress are uneven, which makes the possibility of cracking high from zone 2 to zone 3.

When water quantity decreases in zone 2 and zone 3, the temperature of the slab center increases by about 15°C at the solidification end point, and the length of liquid core increases by about 0.5 m; it has a significant effect on relieving stress concentration. When the proportion of water at the margin is the lowest, the peak value of the first principal stress is also the minimum, and the hot-tearing index decreases. It is obvious when the proportion of water on the

fixed side margin of zone 3 is adjusted from 56% to 60%, and the proportion of water on the loose side margin increases from 40% to 45%.

Data Availability

The simulation results used to support the findings of this study are available from the corresponding author upon request.

Conflicts of Interest

The authors declare no conflicts of interest.

Acknowledgments

This work was supported by the National Natural Science Foundation of China (no. 51474143).

References

[1] W. Bleck, W. Wang, and R. Bülte, "Influence of soft reduction on internal quality of high carbon steel billets," *Steel Research International*, vol. 77, no. 7, pp. 485–491, 2006.

[2] R. Nyström and K.-H. Spitzer, "Development of soft reduction at inexa profil for the possibility of increased productivity with maintained or improved product quality," *Steel Research International*, vol. 74, no. 11-12, pp. 700–707, 2003.

[3] W. Rauter, J. Reiter, K. Srienc et al., "Soft reduction at a round bloom caster: implementation and results," *BHM Berg- und Hüttenmännische Monatshefte*, vol. 159, no. 11, pp. 454–460, 2014.

[4] Y. Li, L. Li, and J. Zhang, "Study and application of a simplified soft reduction amount model for improved internal quality of continuous casting bloom," *Steel Research International*, vol. 88, no. 12, Article ID 1700176, 2017.

[5] C. Ji, S. Luo, M. Zhu, and Y. Sahai, "Uneven solidification during wide-thick slab continuous casting process and its influence on soft reduction zone," *ISIJ International*, vol. 54, no. 1, pp. 103–111, 2014.

[6] C. Ji, S. Luo, and M. Zhu, "Analysis and application of soft reduction amount for bloom continuous casting process," *ISIJ International*, vol. 54, no. 3, pp. 504–510, 2014.

[7] C. Wu, C. Ji, and M. Zhu, "Influence of differential roll rotation speed on evolution of internal porosity in continuous casting bloom during heavy reduction," *Journal of Materials Processing Technology*, vol. 271, pp. 651–659, 2019.

[8] C. Wu, C. Ji, and M. Zhu, "Closure of internal porosity in continuous casting bloom during heavy reduction process," *Metallurgical and Materials Transactions B*, vol. 50, no. 6, pp. 2867–2883, 2019.

[9] S. Luo, M. Zhu, and C. Ji, "Theoretical model for determining optimum soft reduction zone of continuous casting steel," *Ironmaking & Steelmaking*, vol. 41, no. 3, pp. 233–240, 2014.

[10] J. Zhang, D. Chen, S. Wang, and M. Long, "Compensation control model of superheat and cooling water temperature for secondary cooling of continuous casting," *Steel Research International*, vol. 82, no. 3, pp. 213–221, 2011.

[11] K. Ondrejkovič, P. Noga, L. Tkac, G. Hulko, and P. Bucek, "Control of billet temperature field by the secondary cooling in continuous casting of steel," in *Proceedings of the International Conference on Process Control*, IEEE, Strbske Pleso, Slovakia, June 2013.

[12] V. A. Sinelnikov and G. A. Filippov, "Production of high-quality slabs during continuous casting of cracking-sensitive steel: part 2," *Russian Metallurgy (Metally)*, vol. 2014, no. 12, pp. 956–960, 2014.

[13] R. Bülte and W. Bleck, "Formation of internal cracks in steel billets during soft reduction," *International Journal of Minerals Metallurgy and Materials*, vol. 15, no. 2, pp. 114–119, 2008.

[14] J. Garnier, Y. Bréchet, M. Delnondedieu et al., "Irradiation creep of SA 304L and CW 316 stainless steels: mechanical behaviour and microstructural aspects. Part I: experimental results," *Journal of Nuclear Materials*, vol. 413, no. 2, pp. 63–69, 2011.

[15] A. P. Reynolds, W. Tang, T. Gnaupel-Herold, and H. Prask, "Structure, properties, and residual stress of 304L stainless steel friction stir welds," *Scripta Materialia*, vol. 48, no. 9, pp. 1289–1294, 2003.

[16] A. Schmiedt, M. Manka, W. Tillmann, and F. Walther, "Local quasi-static and cyclic deformation behaviour of brazed AISI 304L/BAu-4 joints characterised by digital image correlation," *Welding in the World*, vol. 63, no. 2, pp. 501–509, 2019.

[17] Z. Miaoyong, L. Wentao, W. Weiling et al., "Research progress of numerical simulation in steelmaking and continuous casting processes," *Acta Metallurgica Sinica*, vol. 54, no. 2, pp. 131–150, 2018.

[18] B. G. Thomas, "Review on modeling and simulation of continuous casting," *Steel Research International*, vol. 89, no. 1, pp. 1–21, 2018.

[19] J. Cheng, Y.-X. Wu, Y. Wang, and J.-X. Fu, "Thermo-mechanical analysis of triangular zone cracks in vertical continuous casting slabs based on viscoelastic-plastic model," *Journal of Iron and Steel Research International*, vol. 25, no. 8, pp. 813–820, 2018.

[20] J. Zhang, D.-F. Chen, C.-Q. Zhang, S.-G. Wang, W.-S. Hwang, and M.-R. Han, "Effects of an even secondary cooling mode on the temperature and stress fields of round billet continuous casting steel," *Journal of Materials Processing Technology*, vol. 222, no. 222, pp. 315–326, 2015.

[21] A.-G. Hou, Q.-L. Zhang, G.-D. Xu, and M.-F. Jiang, "Study and application of advanced secondary control model for continuous casting at baosteel," *Journal of Iron and Steel Research International*, vol. 22, no. S1, pp. 98–103, 2015.

[22] H. Feng, L. Chen, Z. Xie, Z. Ding, and F. Sun, "Generalized constructal optimization for solidification heat transfer process of slab continuous casting based on heat loss rate," *Energy*, vol. 66, pp. 991–998, 2014.

[23] H. Fan, M. Long, S. Yu et al., "Uniform secondary cooling pattern for minimizing surface reheating of the strand during round bloom continuous casting," *JOM*, vol. 70, no. 2, pp. 237–242, 2018.

[24] L. Gong, B. Chen, L. Zhang, Y. Ma, and K. Liu, "Effect of cooling rate on microstructure, microsegregation and mechanical properties of cast Ni-based superalloy K417G," *Journal of Materials Science & Technology*, vol. 34, no. 5, pp. 77–86, 2018.

[25] S. Louhenkilpi, E. Laitinen, and R. Nieminen, "Real-time simulation of heat transfer in continuous casting," *Metallurgical Transactions B*, vol. 24, no. 4, pp. 685–693, 1993.

[26] P. F. Kozlowski, B. G. Thomas, J. A. Azzi, and H. Wang, "Simple constitutive equations for steel at high temperature," *Metallurgical Transactions A*, vol. 23, no. 3, pp. 903–918, 1992.

[27] Y.-J. Xia, F.-M. Wang, C.-R. Li, and J.-L. Wang, "Simulation of thermomechanical behavior during continuous casting

process based on MiLE method," *Journal of Central South University*, vol. 19, no. 9, pp. 2403–2410, 2012.

[28] D. S. Bhiogade, S. M. Randiwe, A. M. Kuthe, and A. A. Likhite, "Study of hot tearing in stainless steel CF3M during casting using simulation and experimental method," *International Journal of Metalcasting*, vol. 23, no. 12, pp. 331–342, 2018.

[29] J. Guo and J. Zhu, "Prediction of hot tearing during alloy solidification," in *Proceedings of the 5th Decennial International Conference on Solidification Processing*, pp. 549–553, Sheffield, UK, July 2007.

[30] D. Deng and H. Murakawa, "Numerical simulation of temperature field and residual stress in multi-pass welds in stainless steel pipe and comparison with experimental measurements," *Computational Materials Science*, vol. 37, no. 3, pp. 269–277, 2006.

[31] M. Wu, J. Domitner, and A. Ludwig, "Using a two-phase columnar solidification model to study the principle of mechanical soft reduction in slab casting," *Metallurgical and Materials Transactions A*, vol. 43, no. 3, pp. 945–964, 2012.

[32] T. Takahashi, "Solidification and segregation of steel ingot," *Iron & Steel (China)*, vol. 17, no. 3, pp. 57–61, 1982.

[33] M. M. Wolf, "Definition and control of strand soft reduction," *Current Advances in Materials and Processes*, vol. 11, p. 787, 1998.

[34] J. Cheng, Z. Miaoyong, C. Nailiang et al., "Development and application of dynamic soft reduction control model for slab caster," *Iron & Steel*, vol. 43, no. 9, pp. 38–52, 2008.

[35] T. Nozaki, J.-I. Matsuno, K. Murata, H. Ooi, and M. Kodama, "A secondary cooling pattern for preventing surface cracks of continuous casting slabs," *Transactions of the Iron and Steel Institute of Japan*, vol. 18, no. 6, pp. 330–338, 1978.

[36] Q. Wang and L. Zhang, "Influence of FC-mold on the full solidification of continuous casting slab," *JOM*, vol. 68, no. 8, pp. 2170–2179, 2016.

[37] X. He, P. W. Fuerschbach, and T. Debroy, "Heat transfer and fluid flow during laser spot welding of 304 stainless steel," *Journal of Physics D: Applied Physics*, vol. 36, no. 12, pp. 1388–1398, 2003.

[38] W. Luo, B. Yan, Y. X. Xiong, G. H. Wen, and H. L. Xu, "Improvement to secondary cooling scheme for beam slab continuous casting," *Ironmaking & Steelmaking*, vol. 39, no. 2, pp. 125–132, 2013.

[39] Q. C. Peng, J. J. Wang, and Z. B. Tong, "Study on high-temperature mechanical properties of SPHC steel produced by CSP technology," *Advanced Materials Research*, vol. 1095, pp. 188–192, 2015.

[40] H. Zhang and W. Wang, "Mold simulator study of heat transfer phenomenon during the initial solidification in continuous casting mold," *Metallurgical and Materials Transactions B*, vol. 48, no. 2, pp. 779–793, 2017.

[41] M.-H. Yu, "Advances in strength theories for materials under complex stress state in the 20th century," *Advances In Mechanics*, vol. 55, no. 3, pp. 529–560, 2004.